

Homogeneous Nucleation of Undercooled Al-Ni melts via a Machine-Learned Interaction Potential

Johannes Sandberg^{1,2,4}, Thomas Voigtmann^{1,2}, Emilie Devijver³, and Noel Jakse⁴

¹Institut für Materialphysik im Weltraum, Deutsches Zentrum für Luft- und Raumfahrt (DLR), 51170 Köln, Germany

²Department of Physics, Heinrich-Heine-Universität Düsseldorf, Universitätsstraße 1, 40225 Düsseldorf, Germany

³CNRS, Univ. Grenoble Alpes, Grenoble INP, LIG, F-38000 Grenoble, France

⁴Université Grenoble Alpes, CNRS, Grenoble INP, SIMaP F-38000 Grenoble, France

Abstract

Homogeneous nucleation processes are important for understanding solidification and the resulting microstructure of materials. Simulating this process requires accurately describing the interactions between atoms, which is further complicated by chemical order through cross-species interactions. The large scales needed to observe rare nucleation events are far beyond the capabilities of *ab initio* simulations. Machine-learning is used for overcoming these limitations in terms of both accuracy and speed, by building a high-dimensional neural network potential for binary Al-Ni alloys, which serve as a model system relevant to many industrial applications. The potential is validated against experimental diffusion, viscosity, and scattering data, and is applied to large-scale molecular dynamics simulations of homogeneous nucleation at equiatomic composition, as well as for pure Ni. Pure Ni nucleates in a single-step into an fcc crystal phase, in contrast to previous results obtained with a classical empirical potential. This highlights the sensitivity of nucleation pathways to the underlying atomic interactions. Our findings suggest that the nucleation pathway for AlNi proceeds in a single step toward a B2 structure, which is discussed in relation to the pure elements counterparts.

1 Introduction

The macroscopic properties of a material are closely tied to its microstructure, and understanding their relationship is a central topic in materials science [1]. On a fundamental level, the observed properties originate from the chemical and physical interactions that shape the atomic arrangements and ultimately determine these properties. It is therefore vital to understand the microscopic

nature of crystal nucleation, and growth when the liquid morphs into the solid, if one wants to control the microstructure. Especially, the early steps of the microscopic nucleation process cannot generally be directly observed in experiment, with the very recent exception for Fe-Pt binary metallic nanoparticles by atomic electron tomography [2] that still require to be combined with atomic scale simulations. Often, systems such as colloids [3] are used as model systems studied experimentally for nucleation, still necessitating a computational treatment [4]. Due to the presence of solvent-mediated many-body interactions, it is also not clear whether the kinetic pathways are the same in colloids as in metallic or molecular systems [5]. Simulations at the atomic scale such as Molecular Dynamics (MD) remain one of the dedicated tools that allow for the direct *in silico* study of critical nuclei, their growth, and the local structures in which they emerge from the melt, as reported for generic models as well as metals and alloys [6, 7, 8, 9, 10, 11, 12, 13, 14, 15].

Due to the low probability of observing rare crystal nucleation events, large scale simulations are required. For pure metals and alloys of interest here, empirical or semi-empirical interaction potentials, such as embedded atom models [16, 17], modified embedded atom models [18, 19], and reactive force fields [20], are traditional choices for such simulations, owing to their high performance. There are, however, often large discrepancies between such force fields and experimental results [21, 4]. A better approximation can in principle be achieved by first-principles approaches. *Ab initio* simulations based on Density Functional Theory (DFT) [22, 23], through Car-Parrinello *ab initio* molecular dynamics (AIMD) [24, 25], provide a more faithful representation of the interatomic interaction. Those *ab initio* simulations enable the accurate study of arbitrary mixtures of species in various phases, and have seen success across much of material physics [26, 27, 28, 29, 30, 31, 32, 33, 34, 35, 36]. Unfortunately, computational cost and poor scaling with system size put *ab initio* simulation at odds with the large scale required for observing rare nucleation events.

Machine Learning Interatomic Potentials (MLIPs) were introduced to overcome the limitations of both classical potentials, and *ab initio* simulations. Since the seminal work of Behler and Parrinello [37], a wide range of methods for constructing data-driven potentials have been proposed. These range from linear-regression-based models [38, 39, 40, 41], kernel-based methods such as Gaussian approximation potentials [42, 43, 44], descriptor-based neural network approaches such as the Behler-Parrinello High Dimensional Neural Network Potentials (HDNNP) [37, 45, 46], Deep Potentials [47], and more recently graph neural network potentials [48, 49]. By fitting a machine-learning regression model to *ab initio* potential energy surfaces, it is possible to effectively interpolate them at a computational cost that is orders of magnitude lower. Molecular dynamics studies of nucleation, which require both accurate potentials capable of representing multiple phases and long, large-scale simulations to capture rare nucleation events, benefit greatly from MLIPs [50, 51].

Al-Ni alloys are known for their mechanical performance, thermal stability, and advanced functional properties, making them versatile in both structural and functional applications. The structural ordering in Al-Ni melts has therefore drawn a lot of interest over the past decades, aimed

at understanding the structure-dynamics relationship, and in particular the impact of chemical short-range ordering [52, 53, 54, 55, 56, 57, 58]. Meanwhile, the challenges of experimentally measuring Al self-diffusion coefficients make MD simulations a vital tool for studying this system, and Al alloys more broadly. Molecular dynamics simulations using the first EAM potential by Mishin [59] were used to study self and inter diffusion in Al-Ni across various compositions. These simulations [56] found different diffusivities between the two species, even in Ni-rich compositions, in contrast to the *ab initio* results of [58]. Recently, classical simulations using a new version of the EAM potential of Mishin [60] investigated nucleation into the bcc-based B2 structure at equiatomic composition, and the two-step nucleation of pure Ni into fcc via bcc precursors driven by local icosahedral ordering [14]. Nucleation at AlNi and AlNi₃ compositions were studied using a novel structure identification technique, showing a two-step process for the Ni-rich composition, where chemical ordering of the final phase appearing before bond-orientational ordering during nucleation onset [61].

A reliable description of early stages of crystal nucleation requires an accurate description of the structural and the diffusion in the liquid as well as the crystalline states. Improvement of the interatomic interactions in Al-Ni alloy at the *ab initio* accuracy can be achieved in the framework of machine learning, which has proven to be able to tackle nucleation phenomena for pure aluminium [51].

In the present work, homogeneous crystal nucleation pathways are studied for Al₅₀Ni₅₀ as well as pure Ni. For this purpose, a HDNNP [46] is first trained on AIMD trajectories for Al-Ni alloy in the the whole composition range including pure Ni and pure Al, in the liquid states above and below the melting point as well as relevant crystalline phases at low temperatures. The trained potential is first successfully validated on the local structure as well as self- and inter-diffusion, examining the temperature and composition dependence. Homogeneous nucleation under deep undercooling is then investigated with these potentials by means of large-scale MD simulations with 135000 atoms for the two compositions. For the equiatomic composition a single-step solidification process into the B2 phase is observed. Such a nucleation pathway is discussed in view of the nucleation of their pure elements counterparts. Furthermore, in all the cases nuclei show a relatively irregular, non-spherical shape, different from what is assumed in Classical Nucleation Theory (CNT).

The remaining part of the paper is organized as follows. Section 2 describes the construction of the MLIP and the various properties of interest in the present work. Section 3 is devoted to the validation of the potential as well as the analysis of homogeneous nucleation for the two compositions as well as pure Ni. The conclusions are provided in Section 4.

2 Computational background

2.1 Dataset: *Ab initio* molecular dynamics trajectories

Care must be taken in designing a dataset from *ab initio* calculations, to ensure that the configurations added to the dataset are representative of those encountered during a molecular dynamics run. A straightforward way of doing this is to perform an *ab initio* molecular dynamics simulation, and sampling the resulting trajectories.

All AIMD trajectories were built in the *Vienna Ab Initio Simulation Package* (VASP) [62] within the canonical ensemble, with constant number of atoms N , constant volume V , and constant temperature T (NVT), the average temperature being fixed using a Nose-Hoover thermostat [63, 64]. The dynamics were performed by solving numerically Newton’s equations of motion using the Verlet algorithm in the velocity form with a timestep of 1.5 fs. The electronic system was treated with electron-ion interactions represented by the projector augmented wave (PAW) potentials [65, 66] and exchange and correlation effects were taken into account with the Generalized Gradient Approximation (GGA) [67] in the Perdew, Burke, and Ernzerhof (PBE) [68] formulation. The cutoff energy in the plane-wave expansion was taken as 300 eV. For such large supercells and in the liquid state, only the Γ point was used for sampling the Brillouin zone.

The dataset used in this work was constructed in such a way, with configurations drawn from a number of *ab initio* simulations performed specifically for this task. The majority of these simulations were performed at Ni compositions $x_{\text{Ni}} = 0.25, 0.5, \text{ and } 0.75$, as well as pure Ni, and pure Al, with the aim of covering the entire composition range. For each composition, two branches of simulations were performed, one starting from a high temperature liquid, quenching in steps of 200 K, and one branch starting from a 10 K crystalline state obtained from the *materials project* database [69], and increasing the temperature in steps of 200 K. These simulations were carried out for 60 ps, with some of the liquid alloy simulations continued up to 90 ps in order to ensure that the correct chemical ordering appears and is included in the dataset. A few runs were also performed at a higher pressure, at high temperature, to probe the short-range interaction, and improve the stability of the trained potential. In addition to these primary simulations in the liquid state, additional simulations were performed at 10 K for the stable Al_3Ni_5 , Al_4Ni_3 , and Al_2Ni_3 crystalline phases. The five unstable states on *materials project* closest to the convex hull were included in the same way, namely mp-1183232, mp-1228868, mp-1025044, mp-1229048, and mp-672232. Figure S1 in the supplementary information file shows the x_{Ni} - T locations of the AIMD trajectories as well as the number of configurations sampled from each of them.

2.2 High Dimensional Neural Network Potentials

With the *ab initio* dataset in place, the next step is to define the machine learning model used to construct our MLIP, here the Behler-Parinello HDNNP [37, 45]. In this framework the potential

energy of the many-body system is given *via* a nearsightedness approximation,

$$U \approx \sum_{i=1}^N U_i, \quad (1)$$

where N is the number of atoms in the system, and U_i gives the local energy contribution of atom i , dependent only on atoms j within some neighborhood $r_{ij} = |r_j - r_i| < r_c$ defined by some cutoff distance r_c . In the Behler-Parinello HDNNP approach, U_i is chosen as a species-dependent neural network, taking as input an atomic fingerprint, here given by the Behler-Parrinello Symmetry Functions (SFs)[70]:

$$G_i^2 = \sum_j e^{-\eta(R_{ij}-R_s)^2} f_c(R_{ij}) \quad (2)$$

$$G_i^5 = 2^{1-\zeta} \sum_{j,k} (1 + \Lambda \cos \theta_{ijk})^\zeta e^{-\eta(R_{ij}^2+R_{ik}^2+R_{jk}^2)} f_c(R_{ij}) f_c(R_{ik}) f_c(R_{jk}) . \quad (3)$$

Here, R_{ij} is the distance between atoms i and j , θ_{ijk} is the angle between atoms j and k with respect to atom i , and $f_c(R_{ij})$ is defined as 0 for $R_{ij} > r_c$ and for $R_{ij} < r_c$ as a polynomial going smoothly to 0 at the neighborhood cutoff $R_{ij} = r_c$. The parameters η , ζ , Λ , and R_s allow for defining a set of features by assigning to these parameters different values.

Once the number of SFs used for each species, their parameters, as well as the architecture of the NNP of each species, were chosen, the weights and biases of the NNPs are optimized by minimizing the mean-square error of the HDNNP predictions, with respect to the *ab initio* training dataset. A validation dataset and a test dataset are considered, independent of the training dataset. The validation set is used to evaluate the extrapolation error, to guide the tuning of hyperparameters, and to decide when to end training as part of early stopping. The test dataset is then used to evaluate the final model, after training is completed. All the settings of the HDNN and the parameters of the SFs can be found in [71].

While the HDNNP fits the potential energy surface, it is often beneficial to fit not only the potential energy, but also its gradients, namely the *ab initio* forces. In this work, however, only the energy was considered for the fitting of our HDNNP model. This is to maintain continuity with our previous work on the solidification of pure Al, as well as to not potentially reduce the accuracy of the energetics, which play an important role in the phenomenon of nucleation. This will also allow for a more straightforward future extension of our previously proposed embedded feature selection method [72] to this multicomponent system. Training itself was performed using the N2P2 package [73, 74].

2.3 Classical simulations and analysis

Classical simulations were performed in LAMMPS [75], using the *ml-hdnnp* plugin provided by N2P2 [74]. Time integration was performed using the velocity Verlet algorithm, with a timestep of 1 fs. Simulations for validating the potential were performed in the NVT ensemble, with temperature fixed by a Nosé-Hoover thermostat, and volume pressure controlled indirectly by fixing the volume. MD simulations of homogeneous nucleation were performed in the NPT ensemble, adding a barostat fixing the pressure to ambient conditions. Visualization of the system, common neighbor analysis, and calculation of the pair-correlation functions were performed using OVITO [76]. Calculation of structure factors were performed using ISAACS [77], and the bond-order parameters were calculated with pyscal [78].

2.4 Structural and dynamic properties

Basic structural information of the melt can be obtained from the pair-correlation functions (PCF) [79, 80]. The partial PCF, $g_{ij}(r)$, gives the probability of finding a particle of type i at a distance r from a particle of type j , and can be obtained from simulation by measuring the number of j particles in a spherical shell of thickness Δr and radius r . The ensemble average $n_{ij}(r)$ then gives

$$g_{ij}(r) = \frac{N_j}{V} \frac{n_{ij}(r)}{4\pi r^2 \Delta r}, \quad (4)$$

with V the volume of the simulation box, containing N_j total number of j particles. A Fourier Transform of these partials leads to the partial structure factors

$$S_{ij}(q) = \frac{1}{N} \left\langle \sum_{k=1}^{N_i} \sum_{l=1}^{N_j} \exp \left[i\mathbf{q} \cdot (\mathbf{r}_k^i - \mathbf{r}_l^j) \right] \right\rangle, \quad (5)$$

written here in the Faber-Ziman form [79]. Weighting the $S_{ij}(q)$ with appropriate scattering lengths from neutron or x-ray diffraction leads to the corresponding total Structure factors $S_N(q)$ or $S_X(q)$.

The self-diffusion of atoms in the melt is obtained *via* the Mean Squared Displacement (MSD) at time t given by

$$R_i^2(t) = \frac{1}{N_i} \sum_j^{N_i} \left\langle [\mathbf{r}_j(t+t_0) - \mathbf{r}_j(t_0)]^2 \right\rangle, \quad (6)$$

where the the sum runs over atoms of species i , $\mathbf{r}_j(t)$ denotes the position of atom j at time t , and $\langle . \rangle$ averages over the initial timestep t_0 . From this quantity, the self-diffusion D_i can be extracted via the Einstein relation

$$D_i = \lim_{t \rightarrow \infty} \frac{R^2(t)}{6t}. \quad (7)$$

The shear viscosity of the system is calculated via a Green-Kubo relation from the stress-stress

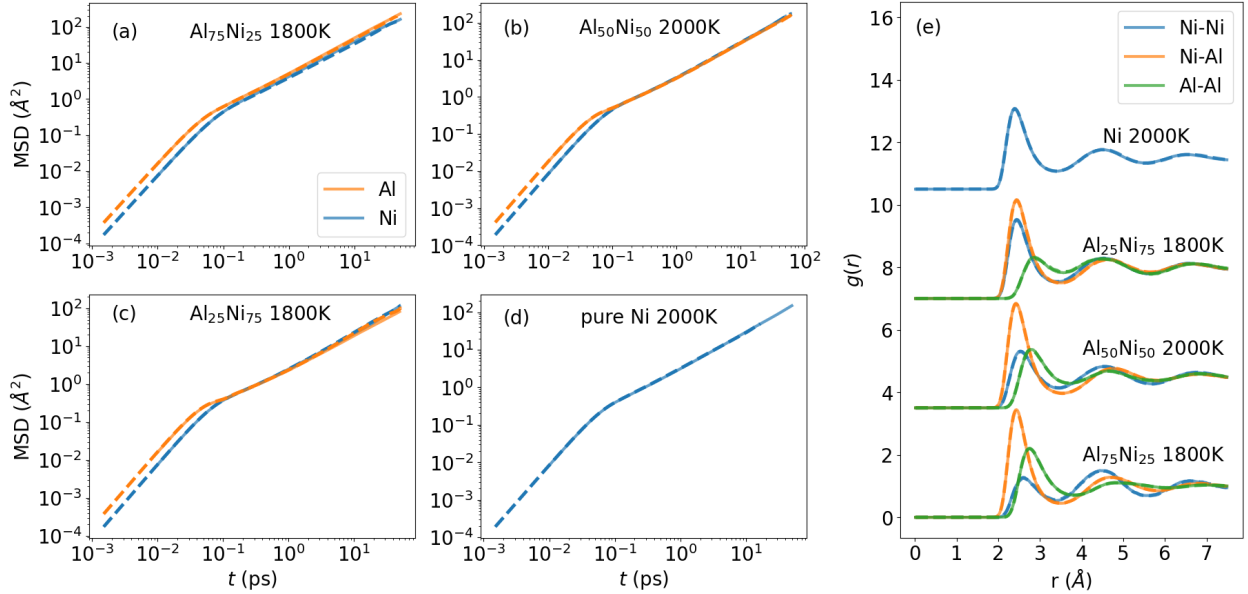


Figure 1: Comparison between NNP and AIMD results for the melt. NNP results are shown as solid lines, AIMD as dashed lines. MSD values are for (a) 1800 K for $\text{Al}_{75}\text{Ni}_{25}$, (b) 2000 K for $\text{Al}_{50}\text{Ni}_{50}$, (c) 1800 K for $\text{Al}_{25}\text{Ni}_{75}$, and (d) 2000 K for pure Ni. PCFs are shown in (e) for the same temperatures, with subsequent compositions shifted upwards by 3.5, 7 and 10.5.

Table 1: Self diffusion coefficients extracted from the mean square displacements in Figure 1 for each Ni composition, x_{Ni} . Values in parentheses are from AIMD.

x_{Ni}	0.25	0.50	0.75	1.0
T (K)	1800	2000	1800	2000
D_{Ni} [$10^{-9}\text{m}^2/\text{s}$]	5.108 (5.578)	5.003 (4.858)	3.884 (3.640)	4.980 (4.977)
D_{Al} [$10^{-9}\text{m}^2/\text{s}$]	7.598 (7.414)	4.527 (4.316)	2.646 (3.043)	-

autocorrelation function

$$\eta = \frac{V}{k_B T} \int_0^\infty dt \langle P_{xy}(t) P_{xy}(0) \rangle, \quad (8)$$

with V the volume of the system, T the temperature, k_B the Boltzmann constant, and $P_{xy}(t)$ the off-diagonal component of the stress tensor at time t . Note that, for an isotropic system, we can average over the xy , xz , and yz components in evaluating the ensemble average.

3 Results and discussion

3.1 Structure and Dynamics

This section is devoted to the validation of the trained HDNNP on the structural properties, such as the pair-correlation functions and the total and partial structure factors, as well as the dynamics

through the self-diffusion coefficients and the viscosity. Comparison with AIMD assesses the quality of the training procedure, while comparison with experiments tests the reliability of the *ab initio* simulation scheme.

As a first evaluation of the potential, the HDNNP is compared to *ab initio* simulations, by performing a set of simulations with $N = 256$ atoms corresponding to the AIMD system size (to exclude finite-size effects in the comparison). A set of configurations were taken from the end of the *ab initio* trajectories as an initial state. The temperature, matching that used in *ab initio*, was chosen to be in the liquid, just above the experimental liquidus line. After initializing the atom velocities according to a Maxwell-Boltzmann distribution, an equilibration of 100 ps was performed, followed by a 200 ps production run.

The mean-square displacements are shown in Figure 1 (a)-(d), along with those calculated from the *ab initio* trajectories. The corresponding values for the self-diffusion coefficients, obtained from the MSD *via* the Einstein relation given by Eq. (7) for both the NNP and for *ab initio* are in good agreement, as shown in Table 1. Note that the largest disagreement occurs for the minority components, Al in $\text{Al}_{25}\text{Ni}_{75}$ and Ni in $\text{Al}_{75}\text{Ni}_{25}$, with other components typically agreeing to within roughly $0.2 \times 10^{-9} \text{m}^2/\text{s}$, which can be seen as a reasonably good agreement.

The partial pair-correlation functions are displayed in Figure 1 (e), and it can be seen that the NNP curves show a nearly perfect match with the AIMD ones. Especially, it reproduces the quite strong affinity between Al and Ni revealed through the large amplitude of the first peak of the Al-Ni partial with respect to the Al-Al and Ni-Ni ones. This indicates a chemical short-range ordering [58] that has a maximum for $\text{Al}_{50}\text{Ni}_{50}$. Table SI of the supplementary information file (SI) shows that for this composition the first peak maximum of the Al-Ni partial is the maximum. All these results highlight the high quality of the training procedure in the whole range of compositions.

A comparison with experimental data is now done through the total and partial structure factors, the temperature and composition dependence self-diffusion coefficients as well as the viscosity. Figure 2(a) shows the structure factor from the HDNNP and compared to the recent neutron diffraction experiments of Belova *et al.* [81] and Maret *et al.* [52]. An excellent agreement is found for the peak positions as well as their amplitudes for all the considered compositions. The partials structure factors in the Faber-Ziman formulation [79] are shown in Figure 2(b) for the four different compositions. For $\text{Al}_{80}\text{Ni}_{20}$, the partials agree remarkably well with the data of Maret *et al.* [52]. Another interesting feature is that the amplitude of the pre-peak of the Ni-Ni partial decreases with increasing Ni composition and is seen to correlate tightly with that of the total structure factor. This suggests that the pre-peak of the total structure factor might originate from the Ni-Ni structural features. It was argued this pre-peak could be a signature of the chemical short-range order [82], and it was later found that it might be characteristic of a medium range ordering [83, 84].

The self-diffusion behaviour with respect to the composition is examined, seeking to match the experimental data points in [55]. At each composition the system is initiated in a 13500 atom fcc

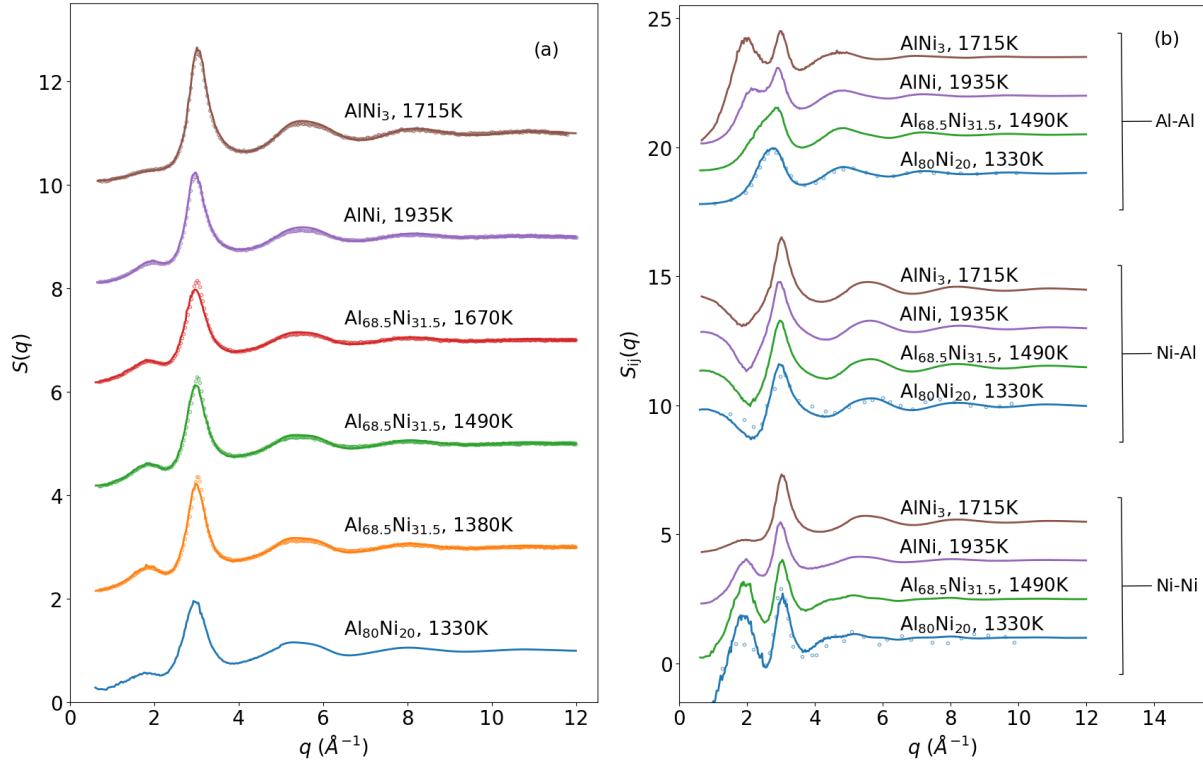


Figure 2: Total structure factor from neutron diffraction for liquid Al-Ni above the liquidus (a), and corresponding Faber-Ziman partial structure factors (b). Comparison between HDNNP (solid lines) and experimental total structure factor [81] (symbols) for $\text{Al}_{25}\text{Ni}_{75}$ at 1715 K, $\text{Al}_{50}\text{Ni}_{50}$ at 1935 K, $\text{Al}_{68.5}\text{Ni}_{31.5}$ at 1700, 1490, and 1380 K. and $\text{Al}_{80}\text{Ni}_{20}$ at 1935 K. The curves are shifted upwards by an amount of 2. The partial structure factors $\text{Al}_{80}\text{Ni}_{20}$ was compared to the experimental data of [52]. The different partials are shifted by an amount of 9 and subsequently shifted by 1.5 for the compositions.

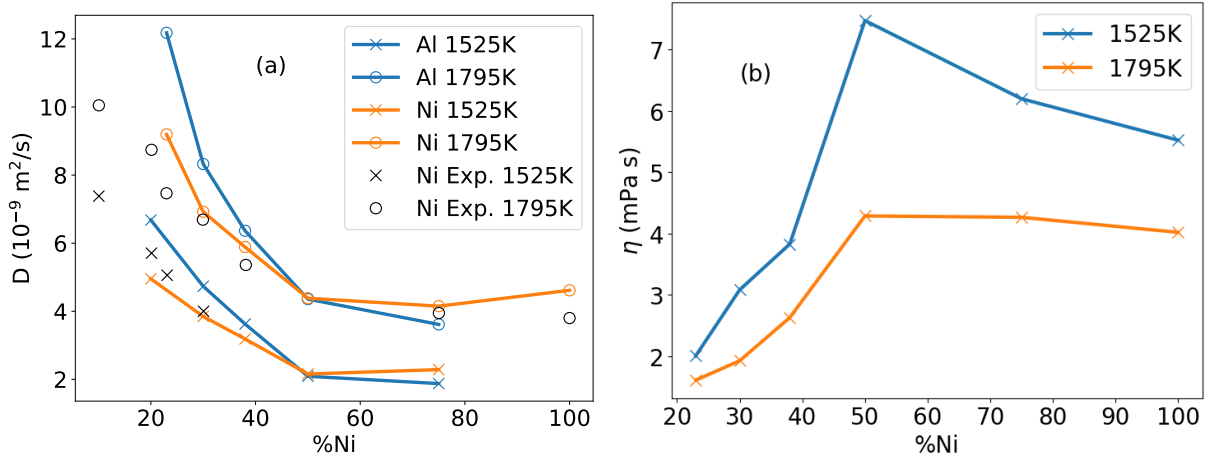


Figure 3: Composition dependence of self-diffusions (a), and viscosity (b), along 1795K and 1525K isotherms. Solid lines show results of this article, with dashed lines showing *ab initio* data of [58], and separate symbols showing experimental data from [55].

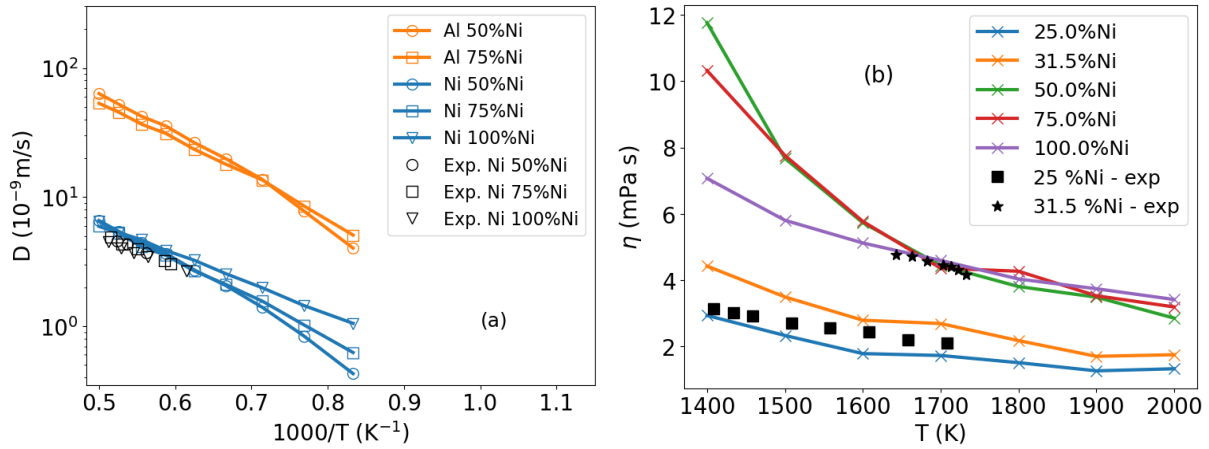


Figure 4: Composition evolution of self-diffusion coefficients (a) and viscosity (b) at ambient pressure for two selected temperatures. Separate symbols show experimental diffusion data from [85], and experimental viscosities from [86].

crystal, with atoms randomly assigned to each species, in the given ratio. The system is then melted at a high temperature of roughly 2000 K for 100 ps, then quenched to the final temperature over 10 ps, and equilibrated for 100 ps, all in a NPT ensemble. Measurements are then performed over 120 ps in a NVT ensemble. Figure 3(a) shows the resulting self-diffusion coefficients, calculated via the Einstein relations. The agreement with the experimental values, shown as separate symbols in the plot, is quite good. A progressive decoupling of the two self-diffusion coefficients sets in as the Ni content decreases above $x_{Ni} = 0.50$. A similar trend was observed in previous AIMD simulations [58]. The same simulation procedure is repeated, in a smaller system of 500 atoms to calculate the viscosity. The latter was calculated *via* the Green-Kubo relation given in Eq. (8), for which each simulation is repeated 10 times to obtain a better ensemble averaging in the calculation of the stress-stress autocorrelation function. Figure 3(b) displays its composition dependence for the two selected temperatures, which shows consistently an opposite trend to the self-diffusion, as expected. It worth mentioning that by decreasing the temperature, a clear maximum occurs at equiatomic composition. This can be understood by the larger Al-Ni affinity for this composition (see Table SI in the SI file) that promotes the compound formation.

A second set of simulations was performed to study the temperature dependence. After being initialized as for the previous set of simulations, the system was quenched in steps of 100 K. At each temperature point a 20 ps equilibration is performed, followed by a 60 ps measurement. The temperature dependence of the self-diffusion coefficients is shown in Figure 4(a). Again, a smaller system is simulated with the same procedure, and used to calculate the viscosities, averaging the stress-stress autocorrelation over 10 realizations before applying the Green-Kubo relations. The viscosities are shown in Figure 4(b). The simulations for the viscosities are also performed at two additional compositions, to compare with existing experimental values of [86], showing a good agreement for $Al_{75}Ni_{25}$, but an underestimation at $Al_{68.5}Ni_{31.5}$.

3.2 Homogeneous Nucleation

With our ML potential at hand, the early stages of crystal nucleation of Al-Ni alloy at equiatomic composition as well as pure Ni are investigated at an unprecedented accuracy. For this purpose, large scale simulations of 135000 atoms were performed. The system is initiated from an fcc solid solution assigning randomly the type of atoms to reproduce $Al_{50}Ni_{50}$ composition. The system is then melted at 2000K, and equilibrated for 100 ps, before being quenched to 1300K with a cooling rate of 13 K/ps, for an undercooling of $\Delta T \approx 650$ K, compared to the experimental liquidus temperature [87]. The simulation is then continued at this deep undercooling, up to 750 ps. All of these simulations were performed at ambient pressure, within an NPT ensemble to observe the onset of nucleation as can be seen in Figure 5, showing a sequence of snapshots of the simulation box at different times.

For all the snapshots, a common neighborhood analysis is performed to classify the local

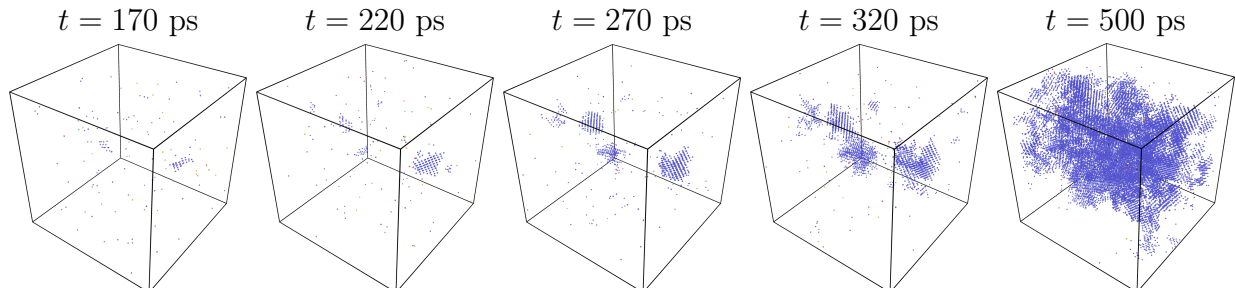


Figure 5: Snapshots of the AlNi system during nucleation, at 170, 220, 270, 320, and 500 ps. Particles are colored according to their CNA signature, blue for bcc, red for hcp, green for fcc, and unidentified atoms not shown.

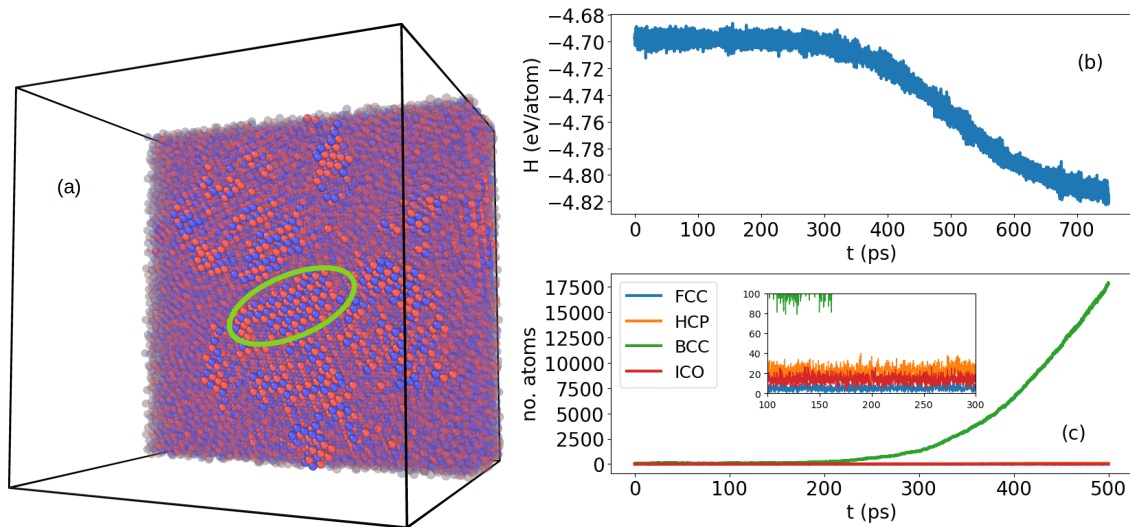


Figure 6: Slice of the simulation box for AlNi during nucleation at 500 ps showing the inner structure of the nuclei in the B2 Structure (a). Enthalpy as a function of time during nucleation (b). Abundance of local structures, identified with the CNA, in the AlNi system (c).

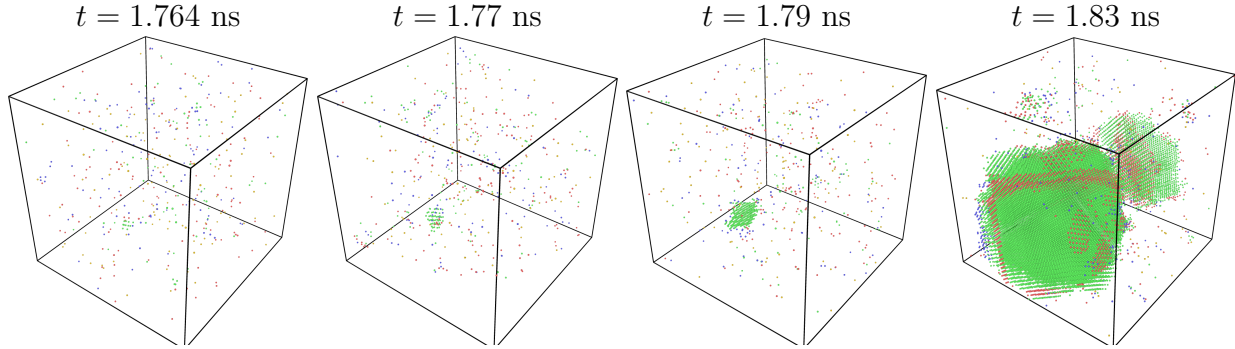


Figure 7: Snapshots of the pure Ni system during nucleation, at 1.76, 1.77, 1.79, and 1.83 ns. Particles are colored according to their CNA structure, blue for bcc, red for hcp, green for fcc, and unidentified atoms being translucent.

topology of atoms. To reduce the influence of thermal noise, before analyzing the configurations, a minimization is applied on each configuration so as to obtain the inherent structures. After an incubation period during which many pre-critical nuclei form and dissolve back into the liquid state, the majority are identified as bcc clusters (colored blue), with only sporadic clusters identified as fcc (green) and hcp (red). Atoms identified as neither of these structures are not shown. Based on visual inspection, we observe nuclei of sizes up to 80 atoms which disappear back into the liquid, putting a lower bound on the critical size n^* . Conversely, the supercritical nuclei appears to arise from clusters to around 120 atoms representing an upper bound to n^* .

Nucleation starts around 170 ps with the growth of a first supercritical nuclei followed by a second one at 220 ps, which is also detected by a sharp drop in the time evolution of enthalpy drawn in Figure 6(b). The nuclei display directly a bcc-type from the beginning of the nucleation as quantified in Figure 6(c), while the fcc and hcp ordering remains always marginal. This indicates a single-step nucleation process directly from the undercooled liquid into the bcc phase. A closer analysis of the inner part of the nuclei as shown in Figure 6(a) indicates clearly a B2 structure. The supercritical nuclei in Figure 5 also shows an apparent non-spherical shape, in contrast to what is assumed in classical nucleation theory [4].

Finally, nucleation pathway of the pure Ni system is investigated. The simulation is performed in the NPT ensemble at ambient pressure with a box of the same size as for $\text{Al}_{50}\text{Ni}_{50}$. Nucleation starts around 1.77 ns after the initial quench from the liquid state at 2000 K to 1200 K, as shown in the snapshots in Figure 7. A CNA analysis on the inherent structures of the snapshots seems to indicate a single fcc nucleus, emerging directly from the melt through a single step process. Analysing the bond-order parameters yields an identical picture, as illustrated by the abundance of different structures shown in Figure 8. Here we observe an increase in fcc structures, with some hcp inclusions corresponding mainly to stacking faults in the fcc crystalline nucleus, that is deemed to disappear in a later stage of the crystallisation. The single-step process observed here is in contrast

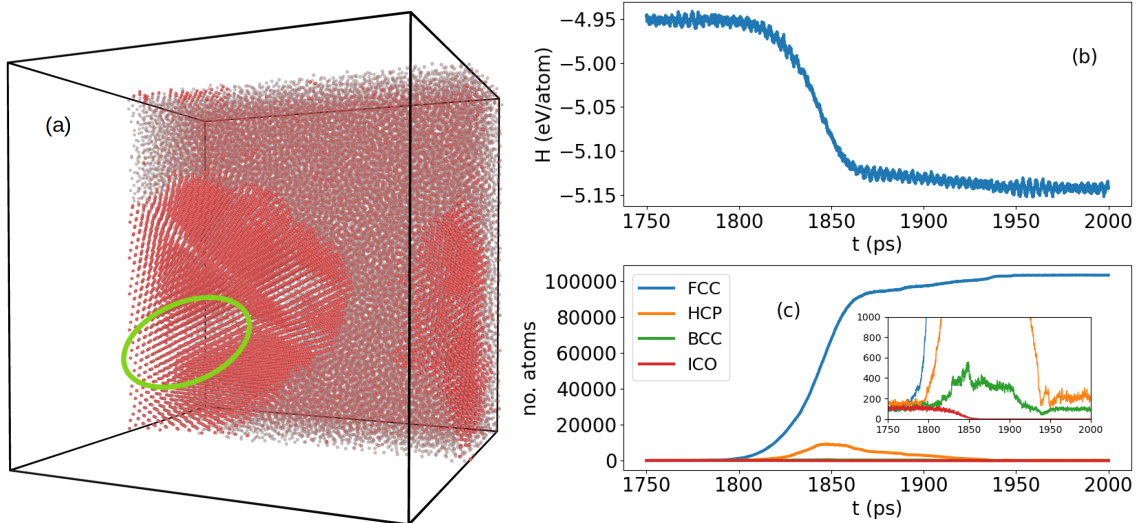


Figure 8: Slice of the simulation box during nucleation at 1.83 ns, showing the fcc structure of the nucleus (a). Enthalpy as a function of time during nucleation (b). Abundance of local structures, identified with the CNA, in the pure Ni system (c).

to the two-step process reported previously by Orihara *et al* [14] using an embedded atom model, but is analogous to the single-step nucleation we have observed for pure Al [51] using a HDNNP for that element.

The fact that $\text{Al}_{50}\text{Ni}_{50}$ nucleates in a B2 crystalline structure despite the fact that the pure elements counterparts, namely Al and Ni, display fcc crystallisation could be understood from the Al-Ni chemical affinity that preexist in the liquid state and is the strongest at equatomic composition, as pointed out in the preceding section. Such an affinity favors the compound formation and the corresponding chemical ordering might take place prior to the topological one when the nucleation takes place as was shown in a previous contribution [61].

4 Conclusion

This work was devoted to the study of homogeneous nucleation of a binary Al-Ni alloy by means of molecular dynamics with a HDNNP trained on AIMD trajectories. A reasonable agreement is found between our simulation results and experimental data in the liquid state for the local structural properties as well as for the dynamics through self-diffusivity and viscosity. We take this as an indication of the reliability of the HDNNP in describing kinetic processes. The thus validated potential allowed us to perform large scale simulations at an unprecedented accuracy for this alloy system, close to the *ab initio* one. Simulation of a highly undercooled equimolar melt shows a single step homogeneous nucleation into a B2 phase. The resulting supercritical nuclei have an irregular shape, in disagreement with the assumptions of the classical theory, and the critical

size is estimated to be between 80 and 120 atoms. In the pure Ni system with the same HDNNP, a single-step nucleation process towards the fcc phase is also seen, in contrast to previous results using EAM. This, at the very least, highlights the sensitive dependence of the nucleation pathway on the details of the underlying interatomic potential.

While the focus was on just two compositions in the present work, the HDNNP is highly accurate for the melt dynamics also over the entire composition range, and thus the nucleation pathways also of other alloy compositions can be studied. We deem it important that the validation occurs against liquid-state transport coefficients: diffusion and interdiffusion are important processes in nucleation and growth, while empirical potentials are often gauged against the equilibrium crystal structures.

Acknowledgments

We acknowledge the CINES and IDRIS under Project No. INP2227/72914, as well as CIMENT/GRICAD for computational resources. We acknowledge financial support under the French-German project PRCI ANR-DFG SOLIMAT (ANR-22-CE92-0079-01). This work has been partially supported by MIAI@Grenoble Alpes (ANR-19-P3IA-0003). JS acknowledges funding from the German Academic Exchange Service through DLR-DAAD fellowship grant number 509. We thank Fan Yang for fruitful discussion on the experimental total structure factors.

References

- [1] Eric J Mittemeijer. Fundamentals of materials science, volume 8. Springer, 2010.
- [2] Jihan Zhou, Yongsoo Yang, Yao Yang, Dennis S Kim, Andrew Yuan, Xuezheng Tian, Colin Ophus, Fan Sun, Andreas K Schmid, Michael Nathanson, et al. Observing crystal nucleation in four dimensions using atomic electron tomography. Nature, 570(7762):500–503, 2019.
- [3] Tian Hui Zhang and Xiang Yang Liu. Experimental modelling of single-particle dynamic processes in crystallization by controlled colloidal assembly. Chemical Society Reviews, 43(7):2324–2347, 2014.
- [4] Gabriele C Sosso, Ji Chen, Stephen J Cox, Martin Fitzner, Philipp Pedevilla, Andrea Zen, and Angelos Michaelides. Crystal nucleation in liquids: Open questions and future challenges in molecular dynamics simulations. Chemical reviews, 116(12):7078–7116, 2016.
- [5] M. Radu and T. Schilling. Solvent hydrodynamics speed up crystal nucleation in suspensions of hard spheres. epl, 105:26001, 2014.
- [6] Stefan Auer and Daan Frenkel. Prediction of absolute crystal-nucleation rate in hard-sphere colloids. Nature, 409(6823):1020–1023, 2001.

- [7] Takeshi Kawasaki and Hajime Tanaka. Formation of a crystal nucleus from liquid. Proceedings of the National Academy of Sciences, 107(32):14036–14041, 2010.
- [8] Søren Toxvaerd. The role of local bond-order at crystallization in a simple supercooled liquid. The European Physical Journal B, 93:1–8, 2020.
- [9] Chunguang Tang and Peter Harrowell. Anomalously slow crystal growth of the glass-forming alloy cuzr. Nature materials, 12(6):507–511, 2013.
- [10] Yasushi Shibuta, Shinji Sakane, Eisuke Miyoshi, Shin Okita, Tomohiro Takaki, and Munekazu Ohno. Heterogeneity in homogeneous nucleation from billion-atom molecular dynamics simulation of solidification of pure metal. Nature communications, 8(1):10, 2017.
- [11] Takuya Fujinaga, Yoshimi Watanabe, and Yasushi Shibuta. Nucleation dynamics in al solidification with al-ti refiners by molecular dynamics simulation. Computational Materials Science, 182:109763, 2020.
- [12] Sébastien Becker, Emilie Devijver, Rémi Molinier, and Noël Jakse. Glass-forming ability of elemental zirconium. Physical Review B, 102(10):104205, 2020.
- [13] Sébastien Becker, Emilie Devijver, Rémi Molinier, and Noël Jakse. Unsupervised topological learning approach of crystal nucleation. Scientific Reports, 12(1):3195, 2022.
- [14] Shunsuke Orihara, Yasushi Shibuta, and Tetsuo Mohri. Molecular dynamics simulation of nucleation from undercooled melt of nickel–aluminum alloy and discussion on polymorphism in nucleation. Materials Transactions, 61(4):750–757, 2020.
- [15] Baoshuang Shang, Noël Jakse, Pengfei Guan, Weihua Wang, and Jean-louis Barrat. Influence of oscillatory shear on nucleation in metallic glasses: A molecular dynamics study. Acta Materialia, 246:118668, 2023.
- [16] Murray S Daw and Michael I Baskes. Embedded-atom method: Derivation and application to impurities, surfaces, and other defects in metals. Physical Review B, 29(12):6443, 1984.
- [17] Murray S Daw, Stephen M Foiles, and Michael I Baskes. The embedded-atom method: a review of theory and applications. Materials Science Reports, 9(7-8):251–310, 1993.
- [18] Michael I Baskes. Modified embedded-atom potentials for cubic materials and impurities. Physical review B, 46(5):2727, 1992.
- [19] Byeong-Joo Lee, Jae-Hyeok Shim, and MI Baskes. Semiempirical atomic potentials for the fcc metals cu, ag, au, ni, pd, pt, al, and pb based on first and second nearest-neighbor modified embedded atom method. Physical Review B, 68(14):144112, 2003.

- [20] Kimberly Chenoweth, Adri CT Van Duin, and William A Goddard. Reaxff reactive force field for molecular dynamics simulations of hydrocarbon oxidation. The Journal of Physical Chemistry A, 112(5):1040–1053, 2008.
- [21] HL Peng, Fan Yang, ST Liu, Dirk Holland-Moritz, Tobias Kordel, T Hansen, and Th Voigtmann. Chemical effect on the structural and dynamical properties in zr-ni-al liquids. Physical Review B, 100(10):104202, 2019.
- [22] Pierre Hohenberg and Walter Kohn. Inhomogeneous electron gas. Physical review, 136(3B):B864, 1964.
- [23] Walter Kohn and Lu Jeu Sham. Self-consistent equations including exchange and correlation effects. Physical review, 140(4A):A1133, 1965.
- [24] Richard Car and Mark Parrinello. Unified approach for molecular dynamics and density-functional theory. Physical review letters, 55(22):2471, 1985.
- [25] Jürgen Hafner. Ab-initio simulations of materials using vasp: Density-functional theory and beyond. Journal of computational chemistry, 29(13):2044–2078, 2008.
- [26] Noël Jakse and Alain Pasturel. Local order of liquid and supercooled zirconium by ab initio molecular dynamics. Physical review letters, 91(19):195501, 2003.
- [27] MMG Alemany, LJ Gallego, and David J González. Kohn-sham ab initio molecular dynamics study of liquid al near melting. Physical Review B—Condensed Matter and Materials Physics, 70(13):134206, 2004.
- [28] Manuel MG Alemany, RC Longo, LJ Gallego, DJ González, LE González, Murilo L Tiago, and James R Chelikowsky. Ab initio molecular dynamics simulations of the static, dynamic, and electronic properties of liquid pb using real-space pseudopotentials. Physical Review B—Condensed Matter and Materials Physics, 76(21):214203, 2007.
- [29] J Souto, MMG Alemany, LJ Gallego, LE González, and DJ González. Ab initio molecular dynamics study of the static, dynamic, and electronic properties of liquid bi near melting using real-space pseudopotentials. Physical Review B—Condensed Matter and Materials Physics, 81(13):134201, 2010.
- [30] Noel Jakse and Alain Pasturel. Liquid aluminum: Atomic diffusion and viscosity from ab initio molecular dynamics. Scientific reports, 3(1):3135, 2013.
- [31] BG Del Rio, LE González, and DJ González. Ab initio study of several static and dynamic properties of bulk liquid ni near melting. The Journal of Chemical Physics, 146(3), 2017.

- [32] Alain Pasturel and Noel Jakse. Atomic-scale structural signature of dynamic heterogeneities in metallic liquids. npj Computational Materials, 3(1):33, 2017.
- [33] Beatriz G Del Rio, Carlos Pascual, Luis E González, and David J González. Structure and dynamics of the liquid 3d transition metals near melting. an ab initio study. Journal of Physics: Condensed Matter, 32(21):214005, 2020.
- [34] MMG Alemany, Jaime Souto-Casares, Luis E González, and David J González. Static structure, collective dynamics and transport coefficients in the liquid li-pb alloy. an ab initio molecular dynamics study. Journal of Molecular Liquids, 344:117775, 2021.
- [35] Alaa Fahs, Philippe Jarry, and Noël Jakse. Structure-dynamics relationship in al-mg-si liquid alloys. Physical Review B, 108(22):224202, 2023.
- [36] Saichao Cao, Mingxu Xia, Noel Jakse, Long Zeng, Pengfei Yu, Yimeng Zhao, Wenquan Lu, and Jianguo Li. Influence of zr element on the atomic structure of al-cu alloy liquid. Scripta Materialia, 248:116143, 2024.
- [37] Jörg Behler and Michele Parrinello. Generalized neural-network representation of high-dimensional potential-energy surfaces. Physical review letters, 98(14):146401, 2007.
- [38] Aidan P Thompson, Laura P Swiler, Christian R Trott, Stephen M Foiles, and Garritt J Tucker. Spectral neighbor analysis method for automated generation of quantum-accurate interatomic potentials. Journal of Computational Physics, 285:316–330, 2015.
- [39] Atsuto Seko, Akira Takahashi, and Isao Tanaka. Sparse representation for a potential energy surface. Physical Review B, 90(2):024101, 2014.
- [40] Akira Takahashi, Atsuto Seko, and Isao Tanaka. Linearized machine-learning interatomic potentials for non-magnetic elemental metals: Limitation of pairwise descriptors and trend of predictive power. The Journal of chemical physics, 148(23), 2018.
- [41] Akshay Krishna Ammothum Kandy, Kevin Rossi, Alexis Raulin-Foissac, Gaétan Laurens, and Julien Lam. Comparing transferability in neural network approaches and linear models for machine-learning interaction potentials. Physical Review B, 107(17):174106, 2023.
- [42] Albert P Bartók, Mike C Payne, Risi Kondor, and Gábor Csányi. Gaussian approximation potentials: The accuracy of quantum mechanics, without the electrons. Physical review letters, 104(13):136403, 2010.
- [43] Albert P Bartók and Gábor Csányi. Gaussian approximation potentials: A brief tutorial introduction. International Journal of Quantum Chemistry, 115(16):1051–1057, 2015.

- [44] Volker L Deringer, Albert P Bartók, Noam Bernstein, David M Wilkins, Michele Ceriotti, and Gábor Csányi. Gaussian process regression for materials and molecules. Chemical Reviews, 121(16):10073–10141, 2021.
- [45] Jörg Behler. Constructing high-dimensional neural network potentials: a tutorial review. International Journal of Quantum Chemistry, 115(16):1032–1050, 2015.
- [46] Jörg Behler. Four generations of high-dimensional neural network potentials. Chemical Reviews, 121(16):10037–10072, 2021.
- [47] Linfeng Zhang, Jiequn Han, Han Wang, Roberto Car, and Weinan E. Deep potential molecular dynamics: a scalable model with the accuracy of quantum mechanics. Physical review letters, 120(14):143001, 2018.
- [48] Kristof T Schütt, Huziel E Saucedo, P-J Kindermans, Alexandre Tkatchenko, and K-R Müller. Schnet—a deep learning architecture for molecules and materials. The Journal of Chemical Physics, 148(24), 2018.
- [49] Simon Batzner, Albert Musaelian, Lixin Sun, Mario Geiger, Jonathan P Mailoa, Mordechai Kornbluth, Nicola Molinari, Tess E Smidt, and Boris Kozinsky. E (3)-equivariant graph neural networks for data-efficient and accurate interatomic potentials. Nature communications, 13(1):2453, 2022.
- [50] Jacek Goniakowski, Sarath Menon, Gaétan Laurens, and Julien Lam. Nonclassical nucleation of zinc oxide from a physically motivated machine-learning approach. The Journal of Physical Chemistry C, 126(40):17456–17469, 2022.
- [51] Noel Jakse, Johannes Sandberg, Leon F Granz, Anthony Saliou, Philippe Jarry, Emilie Devijver, Thomas Voigtmann, Jürgen Horbach, and Andreas Meyer. Machine learning interatomic potentials for aluminium: application to solidification phenomena. Journal of Physics: Condensed Matter, 35(3):035402, 2022.
- [52] M Maret, T Pomme, A Pasturel, and P Chieux. Structure of liquid al 80 ni 20 alloy. Physical Review B, 42(3):1598, 1990.
- [53] N. Jakse, O. Lebacqz, and A. Pasturel. Ab initio molecular-dynamics simulations of short-range order in liquid al₈₀mn₂₀ and al₈₀ni₂₀ alloys. Phys. Rev. Lett., 93:207801, Nov 2004.
- [54] N Jakse, O Le Bacqz, and A Pasturel. Chemical and icosahedral short-range orders in liquid and undercooled al₈₀mn₂₀ and al₈₀ni₂₀ alloys: A first-principles-based approach. The Journal of chemical physics, 123(10), 2005.

- [55] SK Das, J Horbach, MM Koza, S Mavila Chatoth, and A Meyer. Influence of chemical short-range order on atomic diffusion in al-ni melts. Applied Physics Letters, 86(1), 2005.
- [56] Philipp Kuhn, Jürgen Horbach, Florian Kargl, Andreas Meyer, and Th Voigtmann. Diffusion and interdiffusion in binary metallic melts. Physical Review B, 90(2):024309, 2014.
- [57] N Jakse and AJAPL Pasturel. Dynamic properties and local order in liquid al-ni alloys. Applied Physics Letters, 105(13), 2014.
- [58] N Jakse and A Pasturel. Relationship between structure and dynamics in liquid al-ni alloys. The Journal of Chemical Physics, 143(8), 2015.
- [59] Y Mishin, MJ Mehl, and DA Papaconstantopoulos. Embedded-atom potential for b2-ni-al. Physical review B, 65(22):224114, 2002.
- [60] GP Purja Pun and Y Mishin. Development of an interatomic potential for the ni-al system. Philosophical Magazine, 89(34-36):3245–3267, 2009.
- [61] Sébastien Becker, Emilie Devijver, Rémi Molinier, and Noël Jakse. Crystal nucleation in al-ni alloys: an unsupervised chemical and topological learning approach. arXiv preprint arXiv:2210.01894, 2022.
- [62] Georg Kresse and Jürgen Hafner. Ab initio molecular dynamics for liquid metals. Physical review B, 47(1):558, 1993.
- [63] Shuichi Nosé. A molecular dynamics method for simulations in the canonical ensemble. Molecular Physics, 52(2):255–268, 1984.
- [64] William G. Hoover. Canonical dynamics: Equilibrium phase-space distributions. Physical Review A, 31(3):1695–1697, 1985.
- [65] P. E. Blöchl. Projector augmented-wave method. Physical Review B, 50(24):17953–17979, 1994.
- [66] Georg Kresse and Daniel Joubert. From ultrasoft pseudopotentials to the projector augmented-wave method. Physical review b, 59(3):1758, 1999.
- [67] Yue Wang and John P Perdew. Correlation hole of the spin-polarized electron gas, with exact small-wave-vector and high-density scaling. Physical Review B, 44(24):13298, 1991.
- [68] J. P. Perdew and A. Zunger. Self-interaction correction to density-functional approximations for many-electron systems. Physical Review B, 23(10):5048–5079, 1981.

- [69] Anubhav Jain, Shyue Ping Ong, Geoffroy Hautier, Wei Chen, William Davidson Richards, Stephen Dacek, Shreyas Cholia, Dan Gunter, David Skinner, Gerbrand Ceder, et al. Commentary: The materials project: A materials genome approach to accelerating materials innovation. APL materials, 1(1), 2013.
- [70] Jörg Behler. Atom-centered symmetry functions for constructing high-dimensional neural network potentials. The Journal of chemical physics, 134(7), 2011.
- [71] Emilie Devijver Johannes Sandberg, Thomas Voigtmann and Noel Jakse. Homogeneous nucleation of undercooled al-ni melts via a machine-learned interaction potential. Materials Cloud Archive, 10.24435, 2024.
- [72] Johannes Sandberg, Thomas Voigtmann, Emilie Devijver, and Noel Jakse. Feature selection for high-dimensional neural network potentials with the adaptive group lasso. Machine Learning: Science and Technology, 5(2):025043, 2024.
- [73] Andreas Singraber, Tobias Morawietz, Jörg Behler, and Christoph Dellago. Parallel multi-stream training of high-dimensional neural network potentials. Journal of chemical theory and computation, 15(5):3075–3092, 2019.
- [74] Andreas Singraber, Jörg Behler, and Christoph Dellago. Library-based lammmps implementation of high-dimensional neural network potentials. Journal of chemical theory and computation, 15(3):1827–1840, 2019.
- [75] Aidan P Thompson, H Metin Aktulga, Richard Berger, Dan S Bolintineanu, W Michael Brown, Paul S Crozier, Pieter J In't Veld, Axel Kohlmeyer, Stan G Moore, Trung Dac Nguyen, et al. Lammmps-a flexible simulation tool for particle-based materials modeling at the atomic, meso, and continuum scales. Computer Physics Communications, 271:108171, 2022.
- [76] Alexander Stukowski. Visualization and analysis of atomistic simulation data with ovito—the open visualization tool. Modelling and simulation in materials science and engineering, 18(1):015012, 2009.
- [77] Sébastien Le Roux and Valeri Petkov. Isaacs—interactive structure analysis of amorphous and crystalline systems. Journal of Applied Crystallography, 43(1):181–185, 2010.
- [78] Sarath Menon, Grisell Díaz Leines, and Jutta Rogal. pysical: A python module for structural analysis of atomic environments. Journal of Open Source Software, 4(43):1824, 2019.
- [79] W. H. Young. Structural and thermodynamic properties of nfe liquid metals and binary alloys. Reports on Progress in Physics, 55:1769–1853, 1992.

- [80] J. P. Hansen and I. R. McDonald. Theory of Simple Liquids. Elsevier, London, 3rd edition, 2006.
- [81] Irina V Belova, Tanvir Ahmed, Ujjal Sarder, William Yi Wang, Rafal Kozubski, Zi-Kui Liu, Dirk Holland-Moritz, Andreas Meyer, and Graeme E Murch. Computer simulation of thermodynamic factors in ni-al and cu-ag liquid alloys. Computational Materials Science, 166:124–135, 2019.
- [82] Jürgen Brillo, Alexej Bytchkov, Ivan Egry, Louis Henet, Gerhard Mathiak, Irina Pozdnyakova, DL Price, Dominique Thiaudiere, and Didier Zanghi. Local structure in liquid binary al–cu and al–ni alloys. Journal of Non-Crystalline Solids, 352(38-39):4008–4012, 2006.
- [83] OS Roik, OV Samsonnikov, VP Kazimirov, VE Sokolskii, and SM Galushko. Medium-range order in al-based liquid binary alloys. Journal of Molecular Liquids, 151(1):42–49, 2010.
- [84] N Jakse and A Pasturel. Interplay between structural and atomic transport properties of undercooled al-cu binary alloys. AIP Advances, 7(10), 2017.
- [85] Sebastian Stüber, Dirk Holland-Moritz, Tobias Unruh, and Andreas Meyer. Ni self-diffusion in refractory al-ni melts. Physical Review B—Condensed Matter and Materials Physics, 81(2):024204, 2010.
- [86] Iván Egry, Rob Brooks, Dirk Holland-Moritz, Rada Novakovic, Taishi Matsushita, Yuriy Plevachuk, Enrica Ricci, Seshadri Seetharaman, Vasyl Sklyarchuk, and Rainer Wunderlich. Thermophysical properties of liquid al-ni alloys. High Temperatures-High Pressures, 38(4):343–351, 2010.
- [87] H Okamoto. Al-ni (aluminum-nickel). Journal of phase equilibria, 14(2):257–259, 1993.